Available online at www.sciencedirect.com
ScienceDirect
Journal of Solid State Chemistry 181 (2008) 895–904
JOURNAL OF SOLID STATE CHEMISTRY
www.elsevier.com/locate/jssc

Structure, microstructure and magnetic properties of $Sr_{1-x}Ca_xCrO_3$ ($0 \leqslant x \leqslant 1$)

E. Castillo-Martínez[a], A. Durán[a,b], M.Á. Alario-Franco[a,*]

[a]*Departamento de Química Inorgánica, Laboratorio Complutense de Altas Presiones, Facultad de Química, Universidad Complutense de Madrid, EU, 28040 Madrid, Spain*
[b]*Centro de Ciencias de la Materia Condensada, Universidad Nacional Autónoma de México, Apartado Postal 2681, C.P. 22800, Ensenada B.C., Mexico*

Received 10 October 2007; received in revised form 4 January 2008; accepted 7 January 2008
Available online 19 January 2008

Abstract

The effect of the calcium concentration on the structural, microstructural and magnetic properties of $Sr_{(1-x)}Ca_xCrO_3$ with $0 \leqslant x \leqslant 1$ has been studied. The compounds were prepared using high pressure and high temperature synthesis. X-ray diffraction shows that the samples evolve from the cubic *Pm*-3*m* space group for $x = 0$–0.2 to tetragonal *I*4/*mcm* for $x = 0.4$–0.5, then to the orthorhombic *Pbnm* space group for $x = 0.6$, 0.8 and 1.0. Electron diffraction and high-resolution transmission electron microscopy confirmed the respective cells for the end compositions: $\mathbf{a}_p \times \mathbf{a}_p \times \mathbf{a}_p$ (*Pm*-3*m*) for $SrCrO_3$; and the $\sqrt{2}\mathbf{a}_p \times \sqrt{2}\mathbf{a}_p \times 2\mathbf{a}_p$ (*Pbnm*) for $CaCrO_3$. For intermediate compositions some extra spots appear in the electron diffraction patterns while the electron micrographs indicate the presence of microdomains. Magnetic measurements show Curie–Weiss behaviour at high temperature for all the samples. A sharp antiferromagnetic (AFM) transition at about 91.5 K appears for $x = 0.8$–1 together with a weak ferromagnetic ordering below T_N.

Keywords: Perovskite; Cr(IV); Solid solutions; Structure; Microstructure; Electron diffraction; HRTEM; High pressure

1. Introduction

The rich electronic behaviour in perovskite related systems has been known since the end of the 1960s [1], however, some of these compounds were little studied because of the need of high pressure for their synthesis. Among them, the *A*(II)–Cr(IV)–O_3, (*A* = Sr, Ca) perovskite compounds are particularly interesting and have been the subject of recent work [2,3]. In this respect, it is known that the Cr(IV) state in octahedral coordination requires high-pressure conditions to be obtained. In particular, $SrCrO_3$ was stabilized at about 65 kbar and 1023 K [4] while 60 kbar and 973 K were used for obtaining $CaCrO_3$ [5].

Structurally, $SrCrO_3$ (space group (S.G) *Pm*-3*m*) can be described as an undistorted cubic perovskite phase. In contrast, in the $CaCrO_3$ compound, both the relatively small radii of the Ca(II) ion and the consequently increased covalent character of the Ca–O bond distort the perovskite cell. This produces a tilting of the octahedra that originates a lowering of symmetry to an orthorhombic structure (S.G. *Pbnm*).

From the electronic point of view, the original study reported a Pauli paramagnetic behaviour in a $SrCrO_3$ single crystal [4]. Nevertheless, a recent study [2] in polycrystalline samples has not shown the typical metallic behaviour, and this has been attributed to grain-boundary scattering. However, the small thermoelectric coefficient (α) and thermal conductivity (κ) temperature dependence seem to indicate an exotic electronic conduction [2]. Furthermore, susceptibility measurements showed a small splitting of the zero-field cooling (ZFC) and the field cooling (FC) susceptibility curves at about 50 K which seems to be related to weak ferromagnetism as a consequence of the structural distortion mentioned by Williams et al. [3].

On the other hand, the original report for $CaCrO_3$ [5] showed a semiconducting rather than metallic behaviour

*Corresponding author. Fax: +34 91 394 43 52.
E-mail address: maaf@quim.ucm.es (M.Á. Alario-Franco).
URL: http://www.ucm.es/info/labcoap/index.html (M.Á. Alario-Franco).

0022-4596/$ - see front matter © 2008 Elsevier Inc. All rights reserved.
doi:10.1016/j.jssc.2008.01.022

with antiferromagnetic (AFM) ordering at about 90 K. Furthermore, these studies show the existence of an intermediate domain of parasitic ferromagnetism (itinerant electrons) ascribed to antisymmetric exchange interactions in a narrow range between antiferromagnetism (localized electrons) and Pauli paramagnetism (itinerant electrons). Later on, contrary to the original report, Weiher et al. [6] reported metallic character in a $CaCrO_3$ single crystal. Again, the different behaviour was ascribed to the effect of the grain boundary scattering in the polycrystalline sample, since the low Seebeck coefficient imply free charge carriers in the $CaCrO_3$ compound. Furthermore, these authors confirmed the (AFM) transition at about 90 K.

To date, the information about the structural and magnetic properties of $SrCrO_3$ and $CaCrO_3$ is then relatively meagre and, in some cases, contradictory. Furthermore, to our knowledge, the solid solution between $SrCrO_3$ and $CaCrO_3$ has not been studied. In view of the interesting structural characteristics of $A_{(1-x)}A_x'MO_3$ solid solutions [7–10] and considering the rather different magnetic behaviour of the two end members as described above, we have started a study of the $Sr_{1-x}Ca_xCrO_3$ solid solutions. To this end, due to the presence of octahedral Cr(IV), high pressure had to be employed.

In the obtained samples we have performed a detailed powder diffraction study combined with a microstructural analysis using electron diffraction (ED) and high-resolution transmission electron microscopy (HRTEM). The magnetic properties have also been studied. This is described in what follows.

2. Experimental details

The $Sr_{(1-x)}Ca_xCrO_3$ samples with nominal composition $x=0$, 0.2, 0.4, 0.5, 0.6, 0.8 and 1.0 were synthesized at high pressure and high temperature. Different amounts of 99.9% analytical reagents, CrO_2, SrO and CaO were weighed in a dry box to get the expected stoichiometric quantities; they were then thoroughly mixed and introduced into gold capsules for high pressure synthesis, which was performed in a Belt-type apparatus. Several different pressures and temperatures were tested to obtain the main phase in each case. For instance, 65 kbar and 1223 K were the best conditions to obtain the main phase with a minimum amount of impurities for the intermediate values of x. For the end compositions the optimum conditions were 70 kbar and 1073 K for $SrCrO_3$, and 65 kbar and 973 K for $CaCrO_3$.

We have tried to reduce the amount and number of impurities by adding a slight CaO excess, and $KClO_3$. None of them avoided the formation of β-$CaCr_2O_4$. The experiments performed with an excess of CaO led to the formation of $CaCrO_4$ or $Ca_5(CrO_4)_3$. For the samples with a low Ca content we tried the addition of a 5% $KClO_3$ and it yielded $SrCrO_3$ and β-$CaCr_2O_4$ without formation of the substituted perovskite.

X-ray powder diffraction data were collected with a Phillps X'Celerator diffractometer with $CuK_{\alpha 1}=1.54056$ Å radiation equipped with a Ge (111) monochromator, working on the Bragg–Bentano geometry. Data were collected from 5° to 100°, 2θ, for 12 h with a step size 0.0167°. They were refined with the Rietveld method implemented in the Fullprof program [11]. The background was modelled with a linear interpolation between experimental points, while the peak shape was described by a Thompson–Cox–Hastings pseudo-Voigt function convoluted with axial divergence asymmetry function. For impurity phases only the unit cell and profile parameters were refined.

For transmission electron microscopy (TEM) studies, samples were ground under *n*-butanol, and dispersed with ultrasound. A drop of this suspension was evaporated on a copper grid coated with holey carbon. Selected area ED (SAED) was performed in a JEOL 2000FX electron microscope, equipped with a double tilt, ±45°, holder; X-ray energy dispersive spectroscopy (EDS) analyses were also performed *in situ*. HRTEM was carried out in a JEOL 3000FEG electron microscope. ($C_s=0.6$ mm) with a point resolution of 1.7 Å. The magnetic measurements were performed in a quantum design MPMS-SQUID magnetometer. Magnetization versus temperature data were collected in ZFC and FC modes between 2 and 300 K with an applied magnetic field of 0.1 and 1 T. Magnetization vs applied magnetic field (±5 T) was measured at 5 and 35 K.

3. Results and discussion

3.1. Structure analysis from X-ray powder data

The cubic *Pm*-3*m* and orthorhombic *Pbnm* space group were confirmed for the $SrCrO_3$ and $CaCrO_3$ end compositions, respectively, using XRD data and Rietveld analysis. The differences between the end structures are seen by the extra reflections $(111)_o$, $(120)_o$ and $(103)_o$ appearing in orthorhombic $CaCrO_3$ compared to cubic $SrCrO_3$ (Fig. 1b) as well as by the splitting of many parent reflections. The $(200)_c$ splits into $(220)_t$ and $(004)_t$ or $(220)_o$ and $(004)_o$ while the $(222)_c$ re-indexes as $(044)_t$ and splits into $(044)_o$ and $(404)_o$ where the subscripts "c", "t" and "o" correspond to the cubic parent, the tetragonal and the orthorhombic cells, respectively (Fig. 1a). Here, two important facts are clearly observed: (i) as the Ca ion is introduced into the structure, the parent peaks are shifted to higher 2θ values, a result of the smaller Ca^{2+} ion size, and (ii) a peak broadening is seen in the central part of the solid solution. This has two contributions: in the one hand there is the peak splitting, but also, as shown in the refinement there is a proper broadening. In this way, the full-width at half maximum (FWHM) for the $(100)_c=(110)_o$ reflection increases from 0.07°, for $x=0$, up to 0.11° for the $x=0.5$ composition and then decreases again for the other end member ($x=1$). This is usually related to domain size and microstructural

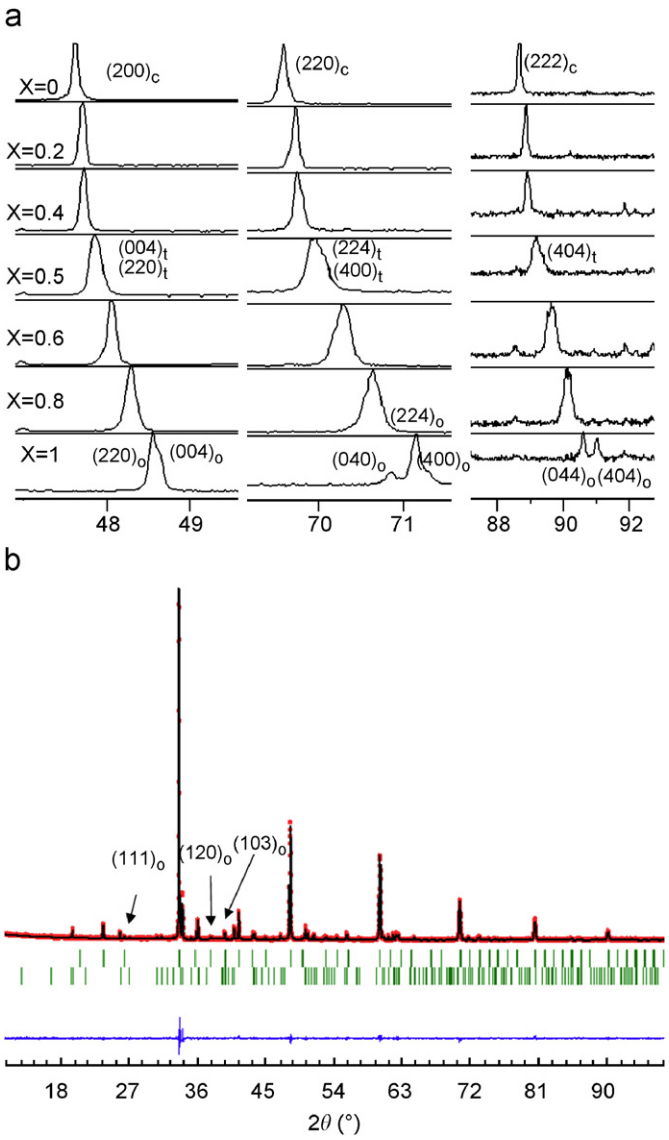

Fig. 1. (a) Evolution with x, of the (200), (220) and (222) parent cubic perovskite reflections for $Sr_{(1-x)}Ca_xCrO_3$ (c = parent cubic, t = tetragonal, o = orthorhombnic). (b) Experimental, calculated and difference X-ray diffraction profile for the sample with nominal composition $x = 0.8$; The $(111)_o$, $(120)_o$ and $(103)_o$ reflections marked with arrows appear due to the orthorhombic symmetry. The observed impurity is β-$CaCr_2O_4$.

changes [12,13]. This is investigated in the microstructural analysis described below.

Initial refinements of the X-ray powder data were performed using the cubic *Pm*-3*m* cell ($\mathbf{a}_p \times \mathbf{a}_p \times \mathbf{a}_p$), where $\mathbf{a}_p$ is the basic perovskite subcell parameter. This structural model gives a good fit for the $x = 0.2$ composition (Table 1). Beyond this, refinements converged poorly and yielded larger R_{WP} and R_B factors, which indicates that the cubic structure is being distorted by the calcium substitution.

For $x = 0.4$, we have considered the 15 Glazer's tilt systems for simple ABO_3 perovskites proposed by Howard and Stokes [14] and found that the experimental observations (XRD, SAED, HRTEM) agree with the requirements for the *I*4/*mcm* space group. Thus, an improvement in the refinements was achieved by changing the space group from *Pm*-3*m* to *I*4/*mcm* for the $x = 0.4$ and 0.5 compositions. This implies that, for these calcium contents, the oxygen octahedra tilt about the *c*-axis results in a so-called diagonal cell $\sqrt{2}\mathbf{a}_p \times \sqrt{2}\mathbf{a}_p \times 2\mathbf{a}_p$. This cell is confirmed by electron microscopy (see below). This symmetry has also been found in other perovskite $Sr_{(1-x)}Ca_xMO_3$ solid solutions, e.g. M = Mn,V [8,15].

For higher Ca concentration (i.e. $x = 0.6$, 0.8 and 1.0) the orthorhombic *Pbnm* S.G. was obtained. An example of the Rietveld refinement is shown in Fig. 1b for the $x = 0.8$ composition. For this symmetry, the cooperative rotations of the octahedra about the cubic [110] axis, do couple additionally to an in-phase tilt about the *c*-axis; this generates a net tilting ($a^-a^-c^+$) about a cubic [111] axis: φ_{111} [16].

The results of the structural refinement are listed in Table 1. The first four rows give information on the lattice parameters at room temperature. The lattice parameters of the end members are in agreement with those reported in Refs. [2–6]. For all investigated compounds some secondary phases, β-$CaCr_2O_4$, Cr_2O_3 and $SrCO_3$ were detected. This suggests that the nominal composition was not really reached. The presence of 5% $SrCO_3$ accompanying $SrCrO_3$ is due to the carbonation of unreacted SrO. The occupation factors of the refinement, rows 7 and 8 in Table 1, indicate that for a full occupancy of the A position, the Ca/Sr ratio is usually lower than the nominal one and the difference decreases with the increase in x. This was also detected in the individual crystals by the EDX technique. Nominal compositions are used to name the respective phases.

The evolution of the lattice parameters as a function of the calcium content in the $Sr_{(1-x)}Ca_xCrO_3$ solid solution is shown in Fig. 2. Three regions are observed, which correspond to the structural changes just mentioned. The first region includes the $0 \leqslant x \leqslant 0.2$ composition (metrically cubic) where the lattice constant decreases from 3.8198(1) to 3.8128(1) Å. By increasing the calcium content, the cubic perovskite changes to an *I*4/*mcm* tetragonal structure. There, the lattice parameters decrease negligibly. Finally, the *Pbnm* orthorhombic structure is obtained in the last region, for the $0.6 \leqslant x \leqslant 1.0$ compositions. As seen in the right side of Fig. 2, the lattice parameters continue decreasing until $CaCrO_3$ is reached, with lattice parameters $\mathbf{a} = 5.2911(1)$ Å, $\mathbf{b} = 5.3192(1)$ Å and $\mathbf{c} = 7.4893(1)$ Å. which are in agreement with those previously reported [2]. Furthermore, the volume of the pseudocubic cell, plotted in the inset of Fig. 2, decreases as the Ca content is increased. It can be seen that it is well above a hypothetical Vegard's law and does not follow a unique path in the whole compositional range. In fact there is a noticeable change in the slope observed at $x = 0.4$ when the structure becomes tetragonal. However, no detectable volume change was observed in the tetragonal-orthorhombic transition at the $x = 0.6$ composition. The observed slope

Table 1
Refined lattice and structural parameters for $Sr_{(1-x)}Ca_xCrO_3$ at 300 K

(x)	0.0	0.2	0.4	0.5	0.6	0.8	1.0
S.G.	*Pm-3m*	*Pm-3m*	I_4/mcm	I_4/mcm	*Pbnm*	*Pbnm*	*Pbnm*
a (Å)	3.8198(1)	3.8128(1)	5.3870(3)	5.3754(2)	5.3553(1)	5.3308(5)	5.2911(1)
b (Å)	3.8198(1)	3.8128(1)	5.3870(3)	5.3754(2)	5.3663(1)	5.3307(5)	5.3192(1)
c (Å)	3.8198(1)	3.8128(1)	7.6208(8)	7.6063(7)	7.5742(2)	7.5468(3)	7.4893(1)
V (Å^3)	55.870	55.428	221.15	219.783	217.66	214.46	210.78
$t_{(SPuDS)}$	1.0033	0.9924	0.9815	0.9760	0.9706	0.9597	0.9488
Sr/Ca							
x	–	–	–	–	−0.0008(20)	0.0113(6)	0.0118(7)
y					0.0016(11)	0.0013(5)	0.0324(4)
N(Sr)	0.125	0.120(1)	0.104(1)	0.084(1)	0.054(1)	0.027(1)	0
N(Ca)	0	0.005(1)	0.022(1)	0.041(1)	0.071(1)	0.098(1)	0.125(0)
O1							
x	–	–	0.260(3)	0.2641(13)	0.729(2)	0.747(3)	0.720(1)
y			0.760(3)	0.7641(13)	0.257(4)	0.287(2)	0.287(1)
z			–	–	−0.003(5)	0.027(11)	0.0319(7)
O2							
x	–	–	–	–	0.057(3)	0.001(5)	0.068(2)
y					0.534(4)	0.555(2)	0.485(2)
B_{iso} (Å^2)	0.21(3)	0.20(3)	0.53(3)	0.22(2)	0.46(3)	0.44(3)	0.022(22)
% β-$CaCr_2O_4$[a]	0	1	11	14	18	20	15
% Cr_2O_3[a]	0	9	0	0	7	0	1
% $SrCO_3$[a]	4.5	0	0	0	0	0	0
R_p (%)	6.3	8.05	6.03	4.05	9.6	8.08	3.71
R_{wp} (%)	8.7	10.3	7.85	5.25	12.5	10.9	4.82
R_B (%)	3.15	6.9	5.69	4.4	3.21	3.27	5.43
X^2	1.57	1.86	2.49	1.52	2.66	1.59	1.59

Atomic positions: S.G. *Pm-3m* (no. 221): Sr/Ca $(\frac{1}{2},\frac{1}{2},\frac{1}{2})$ and Cr (0, 0, 0), O (0, 0, 0.5). S.G. *I4/mcm* (no. 140): Sr/Ca $(0,\frac{1}{2},\frac{1}{4})$, Cr (0, 0, 0), O1 $(x,\frac{1}{2}+x,0)$ and O2 $(0,0,\frac{1}{4})$. S.G. *Pbnm* (no. 62): Sr/Ca 4*c* $(x,y,\frac{1}{4})$, Cr 4*b* $(\frac{1}{2},0,0)$, O1 8d(x, y, z) and O2 4*c* $(x,y,\frac{1}{4})$. N is the refined occupancy factor.
[a]Weight % of impurity phase.

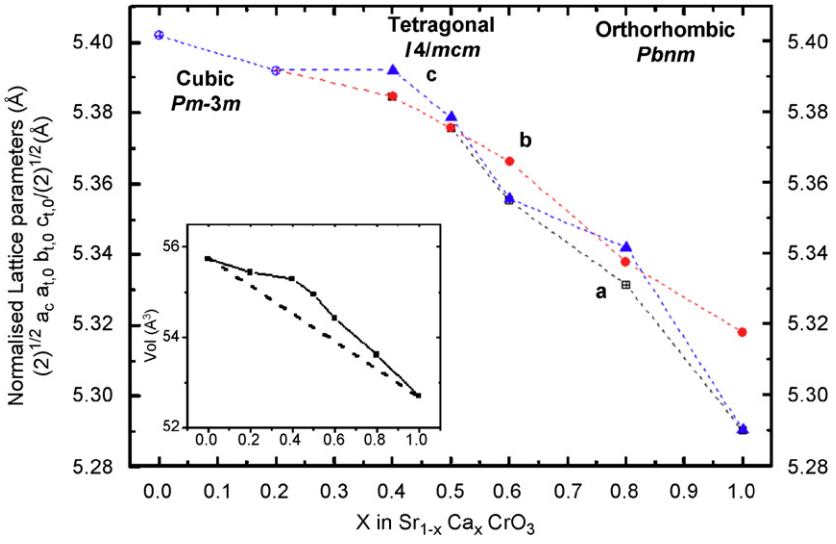

Fig. 2. Normalized unit cell parameters vs composition for $Sr_{(1-x)}Ca_xCrO_3$ ($\oplus a_c$, ■ $a_{o/t}$, ● $b_{o/t}$, ▲ c_o). Lines are guides to the eye. Inset shows the volume of the pseudocubic unit cell ■, with Vegard's Law in a dashed line.

increase in the volume indicates a lowering of the crystal symmetry with respect to the cubic *Pm*-3*m* cell, which is mainly associated to the octahedral tilt that makes the structure more compact.

On the other hand, bond distances, bond angles and tilting angles obtained from the refinement for all compositions are listed in Table 2. Two kinds of nonequivalent oxygen atoms (O1 and O2) appear as a consequence of the lowering in the crystal symmetry. The average Cr–O bond distance, $\langle$Cr–O$\rangle$, is almost constant ~1.91 Å through all the compositions suggesting that the chromium oxidation state is also constant. For this $\langle$Cr–O$\rangle$ distance a radius of 0.56 Å is obtained for Cr, in good agreement with that observed, in general, for Cr(IV) in an octahedral environment [19,20]. At first sight, it would seem that for the end compositions no significant changes are observed in the $\langle$Cr–O$\rangle$ distances, since the observed variation (from 1.910 to 1.908 Å), is quite small suggesting that the total Cr–O bonding interaction is practically constant across the composition. However, a closer look of the data revels that as the Ca content increases, a minimum value of 1.902 Å in the $\langle$Cr–O$\rangle$ distances is observed at $x=0.6$ composition, and then increases to 1.908 Å for $CaCrO_3$. This lengthenning of the $\langle$Cr–O$\rangle$ distance from 0.6 to 1.0 composition is associated to the Jahn–Teller (J–T) distortion in the octahedral enviroment, which is indicated by a long and a short Cr–O1 distance in the equatorial plane and an intermediate Cr–O2 axial distance. This effect has commonly observed in other orthorhombic perovskites [21]. Along with the octahedral distortion, the average Cr–O–Cr angle is continuously reduced from 180° to 158.3°, when the amount of Ca is increased, due to the enhancement of octahedral tilting. This is related to both, the microstructure and the magnetic properties of the compounds.

In conclusion the progressive isovalent substitution of Sr by Ca produces a structural change from the initial cubic, *Pm*-3*m,* perovskite to an intermediate tetragonal, *I*4/*mcm,* structure, and finally to an orthorhombic *Pbnm* structure. This is similar to what has been observed in the closely related systems $Sr_{(1-x)}Ca_xMnO_3$ and $Sr_{(1-x)}Ca_xVO_3$ [8,15]. This behaviour is also consistent with the observation of structural transitions by Zhou et al. [17] in reviewing the series of $REMO_3$ perovskites, (RE = rare earth ion, M = transition metal). They show that when the Goldsmith tolerance factor, t, is close to 1, a structural anomaly occurs and, instead of a smooth transition from cubic (*Pm*-3*m*) to orthorhombic (*Pnma*), an intermediate structure is found. The tolerance factor (t) of each compound of the $Sr_{(1-x)}Ca_xCrO_3$ solid solution is listed in Table 1. The values have been calculated using the software SPuDS [18], which considers the different coordination of the A-cation along the solid solution. Its value is $t>1$ only for the cubic, $SrCrO_3$ and decreases ($t<1$) for the calcium containing phases, passing through the intermediate tetragonal structure before being orthorhombic at $x=0.6$. The fact that the $\langle$Cr–O$\rangle$ distance is almost constant in the solid solution implies that the mismatch between the Cr–O bonds under compression and the Sr,Ca–O bonds under tension when calcium replaces strontium ($t<1$) is relieved by two mechanisms: (1) the cooperative rotations of the $Cr–O_6$ octahedra about the (111) direction, which bend the Cr–O–Cr angles, and shortens the more compressible Sr, Ca–O bonds and (2) the accompanying J–T distortion in the Ca rich samples.

3.2. Microstructure analysis from ED and HRTEM

By means of ED, the reciprocal lattice was obtained for each composition. Fig. 3 shows an example of the evolution of the [−130] zone axis pattern (ZAP), of the cubic perovskite cell, as calcium replaces strontium. In addition to the fundamental perovskite reflections, the appearance of extra reflections with the increase of calcium content can clearly be observed. These reflections appear as a consequence of the lowering of symmetry already detected by X-ray.

The ED pattern of the $x=0$ and 0.2 are apparently similar (Fig. 3a). However, HRTEM showed a $\sqrt{2}\mathbf{a}_p$ lattice parameter and the doubling of the cell along the *c*-axis in many crystals. See for example Fig. 4b. This suggests the existence of a unit cell larger than the basic cubic perovskite ($\sqrt{2}\mathbf{a}_p \times \sqrt{2}\mathbf{a}_p \times 2\mathbf{a}_p$) which could belong to either S.G. I_4/mcm or S.G. Imma. We can therefore conclude that as soon as the Ca enters the cubic structure,

Table 2
Selected bond distances and angles as obtained from the refinement

x	0.0	0.2	0.4	0.5	0.6	0.8	1.0
S.G.	*Pm*-3*m*	*Pm*-3*m*	I4/*mcm*	I4/*mcm*	*Pbnm*	*Pbnm*	*Pbnm*
$Cr–O_1$	1.910(1)	1.906(1)	1.906(16)	1.904(7)	1.947(16)	2.029(11)	1.935(6)
$Cr–O_1$	–	–	–	–	1.849(18)	1.775(13)	1.881(6)
$Cr–O_2$	–	–	1.905(1)	1.902(1)	1.927(3)	1.910(2)	1.909(2)
$\langle$Cr–O$\rangle$	1.910	1.906	1.905	1.903	1.902	1.905	1.908
$Cr–O_1–Cr$	180	180	175.4	173.5	164.06	164.5	158.9
$Cr–O_2–Cr$	–	–	180	180	167.17	162.2	157.7
$\langle$Cr–O–Cr$\rangle$	180	180	176.9	175.7	165.6	163.7	158.3
$\varphi(111)$	0	0	0	0	2.8	10.6	12.5
$\varphi(100)$	0	0	2.3	3.2	–	–	–

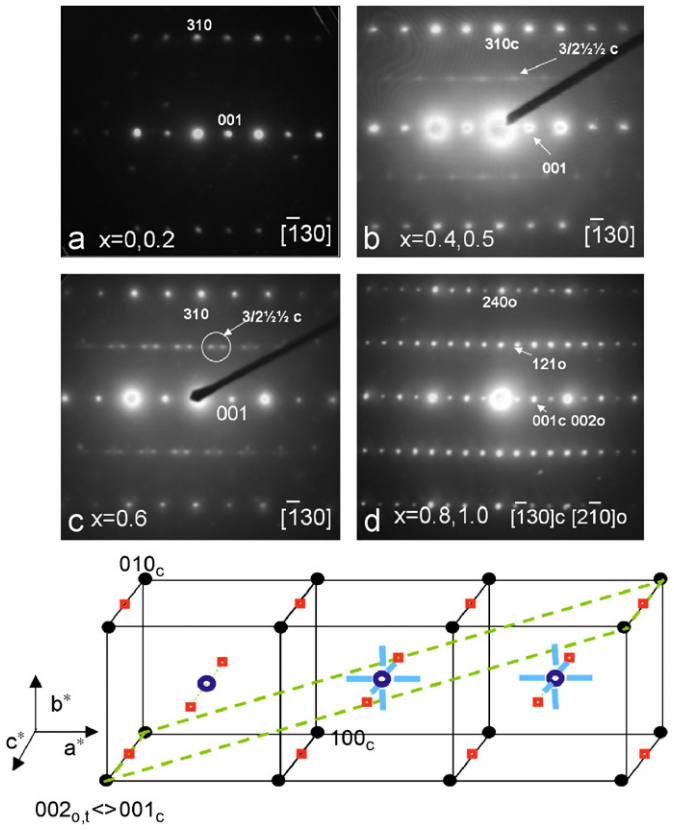

Fig. 3. (a–d) Electron diffraction patterns corresponding to the $[-130]_c$ zone axis of the cubic perovskite subcell equivalent to the $[-210]_o$ of the orthorhombic cell for the compositions: (a) $x = 0$ and 0.2, (b) $x = 0.4$–0.5, (c) $x = 0.6$ and (d) $x = 0.8$ and 1.0. (e) A section of the reciprocal lattice for the $Sr_{(1-x)}Ca_xCrO_3$ solid solution. The different symbols correspond: Solid dots to the cubic subcell ($x = 0$); hollow dark circles to the extra reflections allowed in the tetragonal cell ($x = 0.2$–0.5); light lines to the extra satellites appearing for $x = 0.6$ sample only, the squares complete the full reciprocal lattice of the orthorhombic cell ($x = 0.8$–1.0). The $[-130]_c$ zone axis reciprocal plane is indicated by the dashed parallelepiped.

this is distorted. However, the agreement factors obtained for the Rietveld refinement of the X-ray data did not improve for the tested *I*4/*mcm* S.G. indicating an *average* cubic *Pm*-3*m* space group.

For $x = 0.4$ and 0.5, the reflections (*hkl*), $l = 2n+1$, are clearly observed (Fig. 3c). This confirms the presence of the tetragonal structure. The (121) reflection of the diagonal cell ($\sqrt{2}\mathbf{a}_p \times \sqrt{2}\mathbf{a}_p \times 2\mathbf{a}_p$) is labelled on Fig. 3b as a superlattice reflection (1/3 1/2 1/2) of the cubic perovskite subcell. For $x = 0.6$, onwards, the orthorhombic phase has been used to refine the XRD, but the ED pattern, on Fig. 3c, shows some extra features. There is a clear splitting of the $\frac{1}{2}(hkl)$, $h,k,l =$ odd reflections in a cluster of six satellite reflections in the form of a cross with arms parallel to $\mathbf{g}(100)_p$, $\mathbf{g}(010)_p$ and $\mathbf{g}(001)_p$. where $\mathbf{g}(001)_p$ represents a reciprocal vector along this direction. Obviously, due to the geometry of the Ewald Sphere, in the pattern shown in Fig. 3c, only two of the splitted spots can be observed. This six-fold spot splitting could be due to some Ca/Sr exolution for this composition [22], or to ordering between Ca and Sr probably coupled to the microdomains which formed the system of octahedra tilt [23].

For $x = 0.8$ and 1.0 compositions, the $\frac{1}{2}(hkl)$ reflections become a single spot, $(1/3\ 1/2\ 1/2)_c$, labelled as $(121)_o$ in the orthorhombic setting in Fig. 3d. The superlattice reflections in this composition range become as intense as the fundamental reflections of the perovskite subcell because the orthorhombic cell is now well defined. A summary of the reciprocal lattices for the whole solid solutions have been sketched in Fig. 3e.

The electron micrographs of the different samples give a clear picture of the evolution of the microstructure of the solid solution explaining the concomitant changes in the FWHM with composition described above (Fig. 1). Fig. 4 shows images along the $[100]_c$ zone axis corresponding to samples with different Ca content. The two end members show large areas of homogeneous contrast; $SrCrO_3$ (not shown), is a typical cubic perovskite with no particular features and, on the other hand $CaCrO_3$, (Fig. 4d) shows the doubling of the perovskite subcell. An enlarged image, with the corresponding structure laid over it, is shown in Fig. 4f. Good correspondence between the two is observed. For $x = 1.0$ large perpendicular domains differing in the orientation of the orthorhombic $\mathbf{c} = 2\mathbf{a}_p$ axis were always observed within the same grain. They are in the micron-size range. On the other hand for all the intermediate compositions there is a complex domain microstructure, clearly seen in Figs. 4a–c. This we believe is a rather general phenomenon in this type of systems.

An interesting point resides in the fact that the domain size appears to be composition dependent. For the $x = 0.2$ (Fig. 4a) and 0.8 (Fig. 4c) compositions, a set of three perpendicular, relatively large (≈ 50 A on a side) 3D-microdomains is observed. In each of them the long *c*-axis of the $\approx\sqrt{2}\mathbf{a}_p \times \sqrt{2}\mathbf{a}_p \times 2\mathbf{a}_p$ cell lies along one of the three space directions [24]. In both images, the $2\mathbf{a}_p$ parameter, $\mathbf{c} \approx 7.6$ Å is found at two different orientations and it is perpendicular to the image plane in the areas where the $\sqrt{2}\mathbf{a}_p$ (≈ 5.4 Å) appears [25]. These are marked in the photographs by two parallel white lines. The FFT (insets) are, therefore, composed of the sum of three zone axis as sketched in Fig. 3e. We believe that the presence of microdomains is due to two different facts: (a) the way the samples are prepared; quenched under pressure from high temperature and (b) the small rotation about the [111] axis. As it is observed in Table 2, φ_{111} is below $\sim 13^\circ$. This is within the range of tilt angle in which this type of microdomains are usually observed ($\varphi_{111} \leqslant 20^\circ$) [26].

The $x = 0.5$ sample (Fig. 4b) is particularly interesting since it leads to a more symmetric and random distribution of Sr and Ca ions. The HRTEM image shows no contrast periodicity and not long-range order; this is indicated by the absence of diffraction spots on the fast Fourier transform (FFT) of the whole crystal at $\frac{1}{2}(001)$. (Left inset in Fig. 4b1). This corresponds to space group *I*4/*mcm*, On the other hand, diffuse intensity lines appear along the main direction of the perovskite because of the short-range

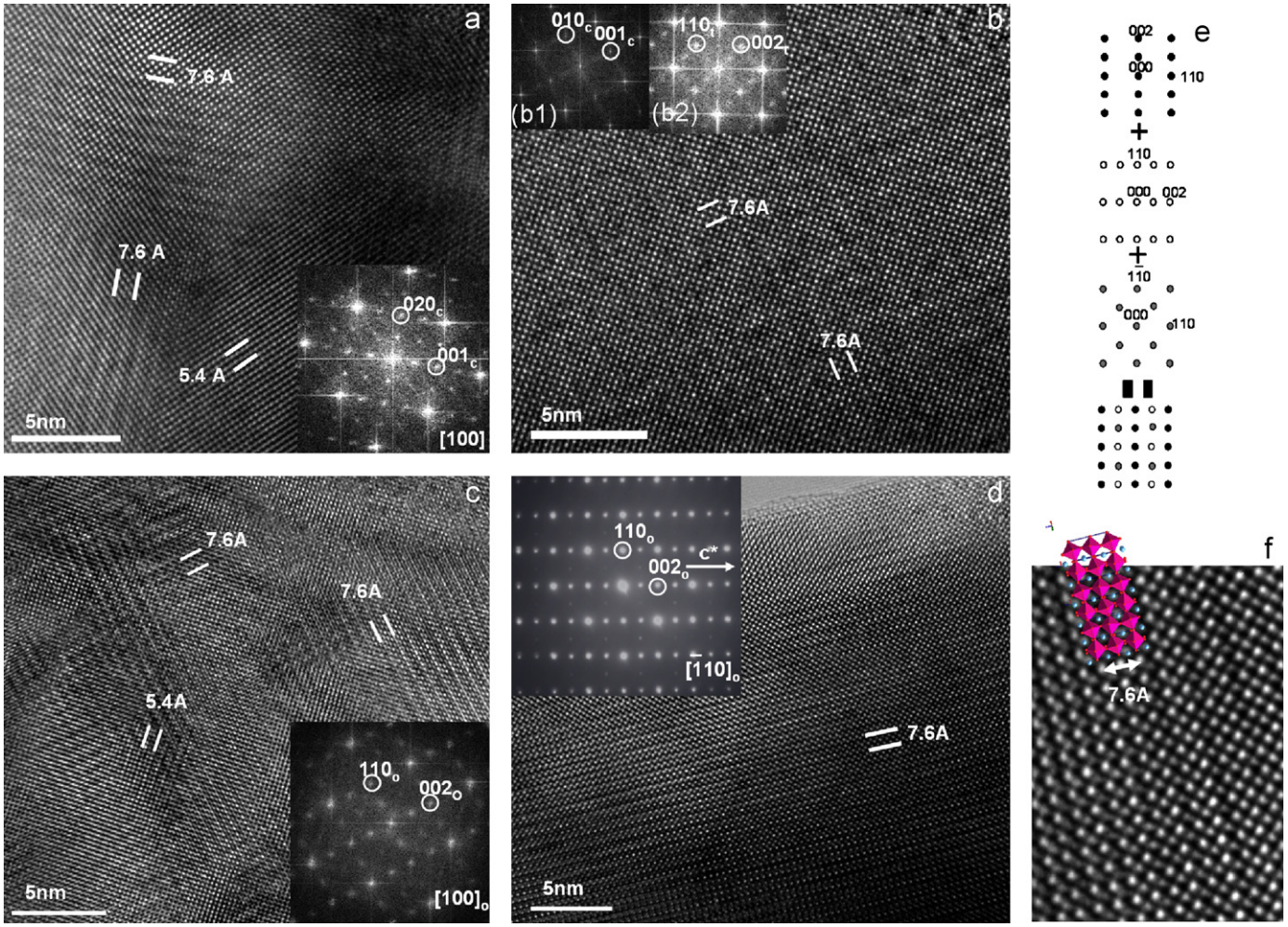

Fig. 4. HRTEM along the [100] axis of the basic perovskite structure for the compositions: (a) $x = 0.2$, (b) $x = 0.5$, (c) $x = 0.8$ and (d) $x = 1.0$. Insets show, respectively, the corresponding FFT in (a–c) and SAED in d. Clearly the domain size changes with the composition (see text). Note that the FFT in Fig. 4b(1 and 2) allows one to distinguish between the global (b1) and the local (b2) diffraction effects. (e) Decomposition of the different domains that contribute to the electron diffraction. (f) Enlargement of the HRTEM of $CaCrO_3$ with the projection of the structure with $\mathbf{c} \approx 2\mathbf{a}_p$ shown.

order. Diffuse intensity effects have also been observed in other Cr(IV) compounds [27]. However, locally the structure is different as shown on the FFT corresponding to a much small area, by the appearance of spots at $\frac{1}{2}(00\ell)$ (right inset in Fig. 4b2) which did not appear in the ED pattern of the crystals. This is in agreement with the short coherence length of the structure repetition in these small domains and, consequently, of the corresponding diffraction effect.

An interesting result out of the HRTEM images is the observation of the dependence of the (micro) domain size with the composition for similar synthesis conditions. Near both end members, domains are bigger than at the centre of the solid solutions range, $Sr/Ca \approx 1$, where domains are clearly much smaller (Fig. 4)

3.3. Magnetic properties

The susceptibility values for all the measured samples are on the same order of magnitude. Fig. 5a shows representative data of the magnetization versus applied magnetic field at 5 K for $SrCrO_3$ compound. As seen in the top left inset, the inverse susceptibility data vs temperature deviates from linearity below 100 K. The data above 150 K are fitted to the Curie–Weiss (C–W) law and the effective magnetic moment, μ_{eff} and the C–W temperature, Θ are found to be 2.98 (± 0.03) μ_B and ~ -315 K, respectively [20], which is in good agreement with the expected value of two localized t_2 electrons in Cr(IV) ion. It is important to note that μ_{eff} value does not agree with the value of $8.3\mu_B$ reported in a recent study where it is attributed to a non-localized electronic state on $SrCrO_3$; [2] this could be due to the contribution of a magnetic impurity or at their sample being off-stoichiometric, likely as consequence of sample washing. However, in the χ^{-1} curve of our sample, a faint anomaly at about 160 K is observed. This anomaly was observed at the same temperature in the thermopower (α) data reported by Zhou et al. [2]. The M vs H data in Fig. 5a), on the other hand, shows two contributions; the linear part above 0.02 T and a faint hysteresis loop in the

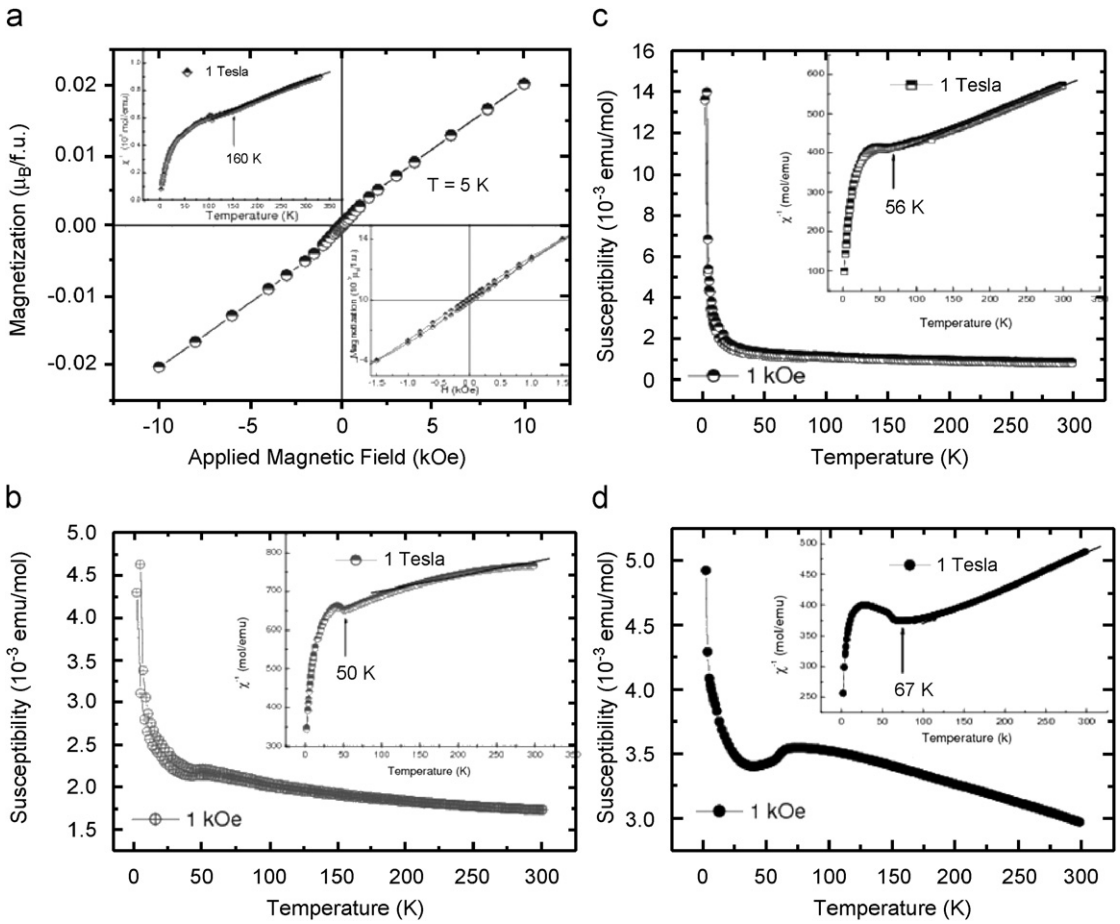

Fig. 5. Magnetic measurements for $Sr_{(1-x)}Ca_xCrO_3$ ($x = 0$–0.5) (a) Magnetization versus the applied magnetic field at 5 K. for $SrCrO_3$. The lower right inset shows the zoom in the low applied field region. The upper left inset shows the inverse of the susceptibility measured at 1 T from 2 to 300 K. (b–d) Susceptibility versus temperature from 2 to 300 K for $x = 0.2$–0.5 samples measured in ZFC and FC mode from 2 to 300 K. The Insets display the inverse of the susceptibility as a function of temperature.

low-field range, $0.02 \leqslant x \leqslant -0.02$ T, as seen in the inset. This is likely due to the weak ferromagnetism as a consequence of the structural distortion pointed out by Williams et al [3].

In order to understand what does happen in the intermediate compositions we plot the $\chi(T)$ data measured with an applied field of 0.1 and the inverse susceptibility, $\chi^{-1}(T)$, at 1 T from 2 to 300 K, for the samples with $0.2 \geqslant x \geqslant 0.8$ of Ca content in Figs. 5b–d and 6a–b. In Figs. 5b and c, one can observe a small anomaly that starts to develop at about 50 and 56 K along with a slight divergence in ZFC and FC modes; this is better seen in the inset of same figures (arrows). This small hump is more pronounced for the $x = 0.2$ sample. Furthermore, for that sample C–W behaviour is roughly observed above 110 K in comparison with the $x = 0.4$ sample, where a linear behaviour is observed above ~150 K. There, the extracted value of μ_{eff} is about 4.54 ($\pm$0.02) and 3.30 ($\pm$0.03) μ_B, and $\Theta \sim -900$ and -470 K for $x = 0.2$ and 0.4, respectively. The susceptibility data for $x = 0.5$, 0.6 and 0.8 are shown in Figs. 5d, 6a and 6b respectively. There, the anomaly is shifted at about 67, 70 and 82 K, respectively, in the inverse of susceptibility data as indicated by arrows in the insets. Above these temperatures, the C–W law fits very well giving values of μ_{eff} ~3.62($\pm$0.01), 3.13 ($\pm$0.01) and ~2.60 ($\pm$0.01) μ_B with $\Theta \sim -540$, -315 and -330 K for $x = 0.5$ 0.6 and 0.8 of Ca content, respectively. Note a small loop in the ZFC and FC when the sample reaches 80% of Ca content. This hysteresis coincides with the AFM transition reported for the end $CaCrO_3$ composition [5,6].

In order to consider the impact of the impurities on the magnetic properties we have prepared a sample of single-phase β-$CaCr_2O_4$ and performed magnetic measurements. It behaves as a C–W paramagnet, with magnetic anomalies at temperatures below those at which the anomalies appear in the $Sr_{(1-x)}Ca_xCrO_3$ compounds. The presence of β-$CaCr_2O_4$ therefore contributes to the magnetic susceptibility increasing the magnetic moment of the paramagnetic region but is not responsible of the observed magnetic anomalies.

In addition to the hysteresis for the $x = 0.8$ composition, the susceptibility also shows other anomalies in the low-temperature region ($T < T_N$), which are better seen in the pure $CaCrO_3$ compound. For this end composition, the

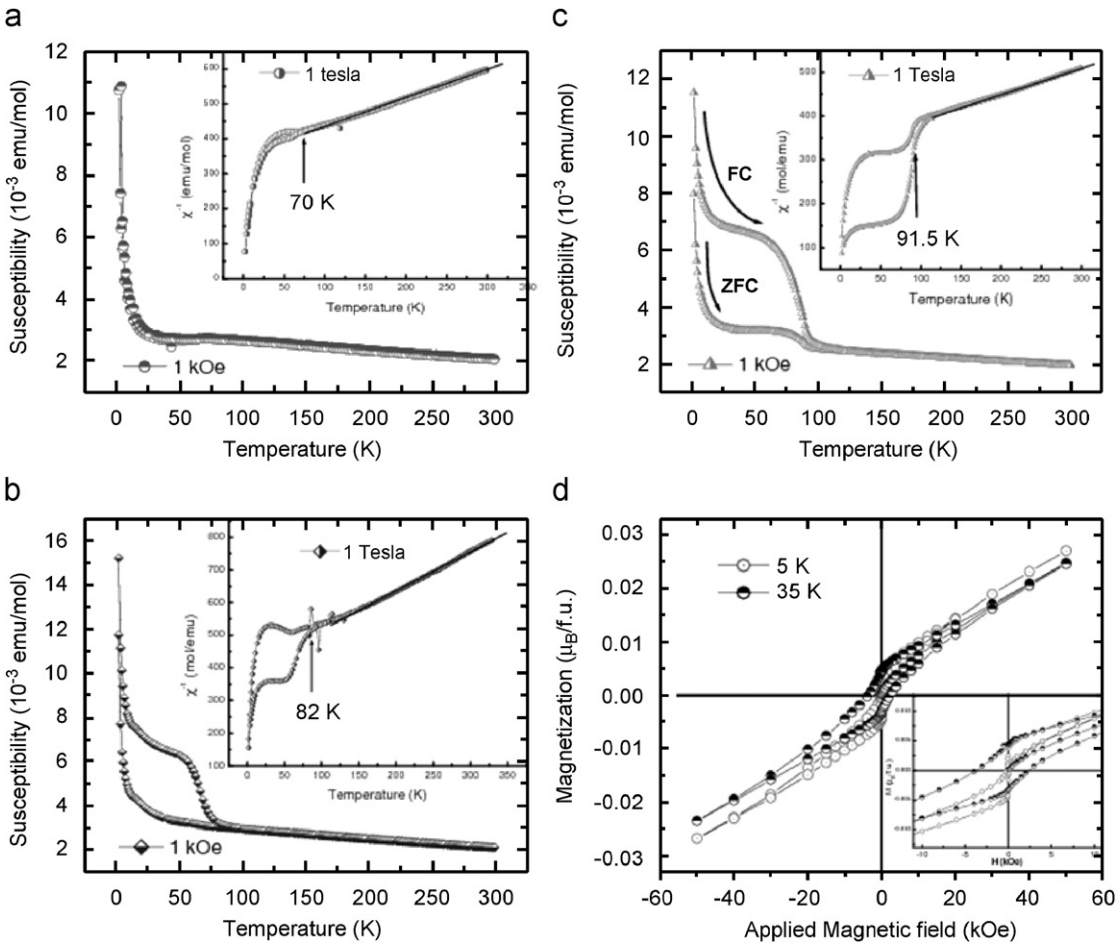

Fig. 6. Magnetic measurements for $Sr_{(1-x)}Ca_xCrO_3$ ($x = 0.5$–1) (a–c) Susceptibility versus temperature for $x = 0.6$, 0.8 and 1, measured in ZFC and FC mode from 2 to 300 K. Insets display the inverse of susceptibility as a function of temperature from 2 to 300 K. (d) Magnetization dependence of the applied magnetic field at 5 and 35 K. The inset shows an expanded scale in the ± 1 T region.

susceptibility and the inverse of susceptibility data at 1 T are shown in Fig. 6c. In order to further understand the low-temperature magnetic anomalies, we also show in Fig. 6d the applied magnetic field-dependent magnetization measurements performed at 5 and 35 K. In addition to AFM ordering at $T_N = 91.5$ K, a weak ferromagnetic (WF) component is seen to develop and it saturates between about 75 and 25 K (seen as a plateau in Fig. 6c). The ZFC susceptibility shows lower saturation values (0.0033 emu/mol) of a weak ferromagnetism than the FC susceptibility (0.0066 emu/mol). The χ^{-1} vs T data shows a sharp drop at 91.5 K, as a consequence of AFM ordering. Furthermore, a linear behaviour above the AFM ordering confirms the C–W behaviour for this composition. The effective moment value of $\mu_{eff} = 3.52$ $(\pm 0.03)\,\mu_B$ (with $\Theta \sim -550$ K) is not far from the theoretical 2.83 μ_B expected from the two localized electrons corresponding to the Cr(IV) ion and very close to the 3.6 μ_B obtained in a single crystal [6]. The weak ferromagnetism is confirmed by the hysteresis loop at 35 K in Fig. 6d. Moreover, when the temperature is lowered to 5 K, the hysteresis loop decreases in size, (inset lower right), supporting the idea that the spin canting and/or the WF domain vanish as the temperature decreases. Extrapolation of the higher field linear region to zero applied field, gives a saturated WF moment of about 0.004 μ_B/f.u. Note also that the coercitivity is higher, and non-symmetric, at 35 K than that observed at 5 K; this implies a non-homogeneous domain magnetic structure or a mixing of non-homogeneous WF and AFM structures coexisting in this range of temperature. This weak ferromagnetism seems to be an intrinsic characteristic for this compound in a narrow range of temperature and appears to cancel upon cooling.

Thus, we can conclude that all samples follow C–W law and show weak magnetic interactions at temperatures that goes from 50 to 90 K with the increase of calcium content. The magnetic behaviour of samples up to $x = 0.6$ seem to be dominated by the properties of the Sr perovskite whereas in the case of $x = 0.8$ and in $CaCrO_3$, when the orthorhombic structure is fully defined, two types of coexisting magnetic domains, AFM and WFM, seem to be present, and the extent of the magnetic interactions could be dependent on the size of the microdomains. A neutron diffraction study is planned to elucidate these results.

4. Conclusions

The $Sr_{1-x}Ca_xCrO_3$ solid solution with $x = 0$, 0.2, 0.4, 0.5, 0.6, 0.8 and 1.0 compositions have been satisfactorily synthesized with the perovskite structure under high pressure and high temperature conditions; these two alkaly metal Cr(IV) oxides, $SrCrO_3$ and $CaCrO_3$ are fully miscible at 60–65 kbars and 900–1000 °C. The cubic perovskite structure accepts the progressive distortion produced by the difference in the A cation size through octahedral tilting, lowering the symmetry at first to *I*4/*mcm* and then to *Pbnm* orthorhombic symmetry. This was observed by XRD and confirmed by ED and HRTEM. For all compositions except $SrCrO_3$, a microdomain structure is formed. Near the end members microdomains are larger than in the middle of the composition range.

All the compounds are C–W paramagnets at high temperature and for Ca rich compositions, $x = 0.8$ and 1.0, they present a sharp transition corresponding to an AFM ordering at about 91.5 K along with WF order extending in a region of temperature below T_N.

Acknowledgments

We thank Angel Arévalo (UCM) for valuable discussions and Dr. J.M. Gallardo Amores for technical assistance. Dr. Pierre Bordet and Dr. Celine Gouyon are acknowledged for allowing the use of their Belt Press for some experiments. We also thank the ''Luis Bru'' Electron Microscopy Center and the X-ray diffraction CAI of UCM. Financial support was funded from CICYT, project MAT2004-01641, Comunidad Autonoma de Madrid, programa MATERYENER, PRICYT S-0505/PPQ-0093 (2006) and Fundación Areces. E. C.-M. acknowledges UCM for a Ph.D. grant.

References

[1] J.B. Goodenough, J.M. Longo, Landolt and Bornstein, vol. III/4a, Part a, Springer, Berlin.
[2] J.S. Zhou, C.Q. Jin, Y.W. Long, L.-X. Yang, J.B. Goodenough, Phys. Rev. Lett. 96 (2006) 046408.
[3] A.J. Williams, A. Gillies, J.P. Attfield, G. Heymann, H. Huppertz, M.J. Martinez-Lope, J. Alonso, Phys. Rev. B 73 (2006) 1004409.
[4] B.L. Chamberland, Solid State Commun. 5 (1967) 663.
[5] J.B. Goodenough, J.M. Longo, J.A. Kafalas, Mater. Res. Bull. 3 (1968) 471.
[6] J.F. Weiher, B.L. Chamberland, J.L. Gillson, J. Solid State Chem. 3 (1971) 529.
[7] S. Qin, A.I. Becerro, F. Seifert, J. Gottsmann, J. Jiang, J. Mater. Chem. 10 (2000) 1609.
[8] Q. Zhou, B.J. Kennedy, J. Solid State Chem. 179 (2006) 3568.
[9] H. Kobayashi, M. Nagata, R. Kanno, Y. Kawamoto, Mater. Res. Bull. 29 (12) (1994) 1271.
[10] E.H. Mountstevens, J.P. Attfield, S.A.T. Redfern, J. Phys Condens. Matter 15 (2003) 8315.
[11] J. Rodríguez-Carvajal, Physica B 192 (1993) 55.
[12] W. Massa, Cryst. Struct. Determination, Springer, Berlin, 2004, pp. 129–130.
[13] R.A. Young, The Rietveld Method, International Union of Crystallography, 1993 (Chapter 8).
[14] C.J. Howard, H.T. Stokes, Acta Crystallogr. B 54 (1998) 782.
[15] J. García-Jaca, J.L. Mesa, M. Insausti, J.I.R. Larrramendi, M.I. Arriortua, T. Rojo, Mater. Res. Bull. 34 (2) (1999) 289.
[16] M. O'Keeffe, B.G. Hyde, Acta Cryst. B 33 (1977) 3802.
[17] J. -S. Zhou, J.B. Goodenough, Phys. Rev. Lett. 94 (2005) 065501.
[18] M.W. Lufaso, P.M. Woodward, Acta Crystallogr. B 57 (2001) 725.
[19] R.D. Shannon, Acta. Crystallogr. A 32 (1976) 751.
[20] E. Castillo-Martínez, M.A. Alario-Franco, Solid State Sci. 9 (7) (2007) 551.
[21] P.M. Woodward, T. Vogt, D.E. Cox, A. Arulraj, C.N.R. Rao, P. Karen, A.K. Cheetham, Chem. Mater. 10 (1998) 3652.
[22] B.S. Guiton, P.K. Davies, Nat. Mater. 6 (2007) 586.
[23] S. García-Martín, F. García-Alvarado, A.D. Robertson, A.R. West, M.A. Alario-Franco, J. Solid State Chem. 128 (1997) 97.
[24] M.A. Alario-Franco, J.M.G. Calbet, M. Vallet, J.C. Grenier, J. Solid State Chem. 49 (1983) 219.
[25] A.J. Dos Santos-García, Myriam H. Aguirre, E. Morán, R. Saez Puche, M.A. Alario-Franco, J. Solid State Chem. 179 (2006) 1296.
[26] A. Vegas, M. Vallet-Regi, J.M. Gonzalez-Calbet, M.A. Alario-Franco, Acta Crystallogr. B 42 (1986) 167.
[27] A.M. Arévalo-López, M.A. Alario-Franco, J. Solid State Chem. 180 (2007) 3271.